

# Stratospheric Age-of-Air: Sensitivity to Finite Volume Remapping Algorithm

Clara Orbe <sup>1,2</sup>, Lawrence L. Takacs <sup>3</sup>, Amal El Akkraoui <sup>3</sup>,  
Krzysztof Wargan <sup>3</sup>, Andrea Molod <sup>3</sup>

<sup>1</sup>NASA Goddard Institute for Space Studies, New York, NY

<sup>2</sup>Department of Applied Physics and Applied Mathematics, Columbia University, New York, NY

<sup>3</sup>Global Modeling and Assimilation Office, NASA Goddard Space Flight Center, Greenbelt, MD

## Key Points:

- The stratospheric mean age-of-air simulated in GEOS-5 is sensitive to the remapping scheme used within the finite-volume dynamical core.
- This sensitivity in the age-of-air approaches 30% and imprints on the simulated distributions of several long-lived chemical trace gases, including nitrous oxide and methane.
- The age-of-air sensitivities primarily reflect changes in resolved wave convergence over the Northern Hemisphere midlatitude stratosphere, which impact mean upwelling within the tropical lower stratosphere.

---

Corresponding author: =name=, =email address=

17 **Abstract**

18 Accurately modeling the large-scale transport of trace gases and aerosols is critical  
 19 for interpreting past (and projecting future) changes in atmospheric composition.  
 20 Simulations of the stratospheric mean age-of-air continue to show persistent biases among  
 21 chemistry climate models, although the drivers of these biases are not well understood.  
 22 Here we identify one driver of simulated stratospheric transport differences among various  
 23 NASA Goddard Earth Observing System Version 5 (GEOS-5) candidate model versions  
 24 under consideration for the upcoming GEOS-5 Retrospective analysis for the 21<sup>st</sup>  
 25 Century (GEOS-R21C). In particular, we show that the simulated age-of-air values are  
 26 sensitive to the so-called “remapping” algorithm used within the finite-volume dynamical  
 27 core, which controls how individual material surfaces are vertically interpolated back  
 28 to standard pressure levels after each horizontal advection time step. Differences in the  
 29 age-of-air resulting from changes within the remapping algorithm approach  $\sim 1$  year over  
 30 the high latitude middle stratosphere - or about 30% climatological mean values - and  
 31 imprint on several trace gases, including methane ( $\text{CH}_4$ ) and nitrous oxide ( $\text{N}_2\text{O}$ ). These  
 32 transport sensitivities reflect, to first order, changes in the strength of tropical upwelling  
 33 which are driven by changes in resolved wave convergence over northern midlatitudes  
 34 as (critical lines of) wave propagation shift in latitude. Finally, we show that degrada-  
 35 tions in the simulation of the age-of-air, stratospheric upwelling and zonal wind climate  
 36 statistics derived from 30-year-long atmosphere-only (AMIP) experiments, translate to  
 37 degraded skill in the analysis states used within data assimilation experiments. Our re-  
 38 sults strongly support continued examination of the role of numerics in contributing to  
 39 transport biases in composition modeling.

40 **Plain Language Summary**

41 Large-scale transport plays a crucial role in distributing climatically important trace  
 42 constituents in the atmosphere, especially in the stratosphere where transport largely  
 43 determines the chemical lifetimes of trace gases. One summary of transport in the strato-  
 44 sphere is the “mean age” or the mean transit time since air at a point in the stratosphere  
 45 was last in the troposphere. Current models used for simulating stratospheric compo-  
 46 sition produce a range of simulated ages, although these differences are poorly under-  
 47 stood. Among other factors, model numerics play a critical role in transport, but few  
 48 studies have explored the sensitivity of the mean age to the choice of numerical scheme  
 49 employed within different dynamical cores. Here we use one model to show that the mean  
 50 age is sensitive to the so-called “remapping” algorithm used within the finite-volume dy-  
 51 namical core that controls how individual material surfaces are vertically interpolated  
 52 back to standard pressure levels after each horizontal advection time step. This reflects  
 53 sensitivities in the representation of how waves propagate from the troposphere into the  
 54 stratosphere. This work suggests that model numerics can be an important factor in con-  
 55 tributing to differences in simulated transport among models.

56 **1 Introduction**

57 The chemical and radiative properties of the troposphere and lower stratosphere  
 58 are strongly influenced by the stratosphere-troposphere exchange of mass and tracers (e.g.,  
 59 Morgenstern and Carver (2001); Hegglin et al. (2006); Pan et al. (2007)). Properly sim-  
 60 ulating the stratospheric circulation and its influence on atmospheric composition in earth  
 61 system models is important for capturing past decadal trends in surface climate, par-  
 62 ticularly in response to changes in Southern Hemisphere ozone depletion (e.g., Son et  
 63 al. (2009); Polvani et al. (2011)). In the Northern Hemisphere (NH), the stratospheric  
 64 circulation’s coupling to ozone could represent an important feedback on the climate’s  
 65 response to future increases in greenhouse gases (GHGs), especially over the North At-  
 66 lantic (e.g., Chiodo and Polvani (2019)). On shorter subseasonal timescales, stratospheric

67 ozone changes associated with strong polar vortex states may also modulate Arctic sea  
68 level pressure and surface temperatures (e.g., Ivy et al. (2017); Oehrlein et al. (2020)),  
69 so much so that seasonal forecast systems employing prognostic ozone show suggestions  
70 of increased signal-to-noise ratio in predictions of the North Atlantic Oscillation (B. M. Monge-  
71 Sanz et al. (2022)).

72 Key to accurately simulating a consistent representation of coupling between strato-  
73 spheric dynamics and chemical trace gases is ensuring that a model’s underlying trans-  
74 port circulation is properly represented. To this end, much effort has been paid to de-  
75 veloping and refining so-called “tracer-independent” metrics of transport (Holzer and Hall  
76 (2000)) such as the mean age-of-air (Hall and Plumb (1994)) and to applying these mea-  
77 sures to rigorously evaluate model transport characteristics in chemistry climate mod-  
78 els (CCMs) (e.g., Hall et al. (1999); Orbe et al. (2018); Dietmüller et al. (2018); Aba-  
79 los et al. (2020)).

80 While the assessment of CCMs participating in the SPARC Chemistry Climate Model  
81 Validation (SPARC CCMVal) effort showed a marked improvement in simulated trans-  
82 port characteristics relative to previous intercomparisons (J. Neu et al. (2010)), more re-  
83 cent analysis of models participating in the SPARC Chemistry Climate Modeling Ini-  
84 tiative (CCMI) (Eyring et al. (2013)) do not demonstrate any improvement (Dietmüller  
85 et al. (2018), see their Figure 3). In particular, although some models produce mean age  
86 values that agree well with observational estimates, the CCMI intermodel spread is ~  
87 50%, with models generally simulating transport that is too vigorous, relative to obser-  
88 vations. While documenting these transport differences among models is straightforward,  
89 understanding the drivers of this spread remains a key challenge and there is still no con-  
90 sensus on the main drivers of simulated age biases among the current generation of CCMs.

91 A key challenge in identifying the drivers of age-of-air – and other stratospheric trans-  
92 port – biases is that they reflect the time-integrated effects of advection by the residual  
93 mean circulation and eddy diffusive mixing, or the quasi-random transport due to the  
94 breaking of Rossby waves (e.g., Holton et al. (1995); Plumb (2002)). Given that the in-  
95 fluences of mixing and advection are not easily separable, studies have come to differ-  
96 ent conclusions about the drivers of age biases in models. In particular, the analysis of  
97 the CCMVal models showed a strong correlation between the intermodel spread in the  
98 age-of-air and lower stratospheric tropical upwelling, whereas Dietmüller et al. (2018)  
99 showed that the age spread among the CCMI models was driven by differences in mix-  
100 ing. While future attempts to further distinguish between these drivers of age biases us-  
101 ing either simplified “leaky pipe” models (Plumb (1996); J. L. Neu and Plumb (1999))  
102 or more complete measures of the transport circulation such as the “age spectrum” (e.g.,  
103 Hall and Plumb (1994); Waugh and Hall (2002))) may prove enlightening, at present there  
104 is no consensus on what is driving biases in the simulated age-of-air in models.

105 One potential limitation of using multi-model intercomparisons to understand drivers  
106 of age biases is that many aspects of model formulation can influence both stratospheric  
107 upwelling and mixing. Thus, while intercomparisons are useful for identifying common  
108 model biases, understanding the drivers of these biases is difficult absent single model-  
109 based process studies. Among these, several aspects of model formulation have been iden-  
110 tified as influencing simulated mean age distributions. As the mean age is sensitive to  
111 vertical motion in the lowermost stratosphere, these include large sensitivities to verti-  
112 cal resolution (Orbe et al. (2020)) and to spurious vertical mixing either introduced in  
113 vertical coordinate transformations in offline chemical transport models (B. Monge-Sanz  
114 et al. (2007)) or through use of assimilated winds performed either in offline (e.g., Legras  
115 et al. (2004)) or online data assimilation and “nudged” configurations (e.g., Pawson et  
116 al. (2007); Orbe et al. (2017); Davis et al. (2022)). These age sensitivities can be still fur-  
117 ther amplified, depending on whether or not parameterized gravity waves are included  
118 (Eichinger et al. (2020)).

119 By comparison, sensitivities of the mean age to underlying tracer numerics have  
 120 been less well examined, although Eluszkiewicz et al. (2000) documented a large sensi-  
 121 tivity in simulated age-of-air values to the choice of advection scheme. More recently,  
 122 Gupta et al. (2020) showed differences of  $\sim 25\%$  in the age-of-air across identical exper-  
 123 iments performed using four different dynamical cores, especially between those using  
 124 spectral versus finite-volume schemes. The experiments employed in that study, how-  
 125 ever, were highly idealized and it is not clear if the strong influence of tracer numerics  
 126 that they identified is also realized in more comprehensive model simulations with moist  
 127 physics, especially in the context of model development as carried out in operational mod-  
 128 eling centers.

129 To this end, here we document the sensitivity of the stratospheric mean age in sev-  
 130 eral recent versions of the NASA Goddard Earth Observing System Version 5 (GEOS-  
 131 5) general circulation model (Molod et al., 2015) that represent different stages in model  
 132 development since MERRA-2 (Gelaro et al. (2017)). Our focus on transport evaluation  
 133 is in wake of the upcoming release of the GEOS-5 Retrospective analysis for the 21<sup>st</sup> Cen-  
 134 tury (GEOS-R21C), which will serve as an intermediate reanalysis between MERRA-  
 135 2 and MERRA-3 ( $\sim 2025$ ). As GEOS-R21C will be used to drive an off-line chemistry  
 136 reanalysis (GEOS-R21C-Chem) it is imperative that it produces a credible representa-  
 137 tion of transport processes.

138 In particular, here we document how in the process of evaluating candidate sys-  
 139 tems for GEOS-R21C we found that the mean age was  $\sim 1$  younger than the values sim-  
 140 ulated in the model version used to produce MERRA-2 (Figure 1). The model versions  
 141 shown in Figure 1 reflect more than 10 years’ worth of accumulated changes in model  
 142 development, most notably changes in radiation, parameterized convection and, as we  
 143 focus on here, changes in the algorithm used to transform advected fields from Lagrangian  
 144 levels to fixed pressure levels after each horizontal advection time step. We show that  
 145 slight modifications in this so-called “remapping” algorithm are the primary driver of  
 146 the age-of-air changes exhibited in recent GEOS-R21C candidate model versions, a re-  
 147 sult which may have broader implications for other general circulation models using fi-  
 148 nite volume (FV) dynamical cores. We begin by discussing methods in Section 2 and present  
 149 key results and conclusions in Sections 3 and 4, respectively.

## 150 2 Methods

### 151 2.1 Model Configurations

152 Here we present results from several versions of GEOS-5 spanning MERRA-2 to  
 153 more recent candidates for GEOS-R21C. Among these model versions, a subset are more  
 154 “official” as they have been documented and/or employed in recent model intercompar-  
 155 isons and are highlighted in Figure 1. In particular, these include an intermediary model  
 156 version that was used in Phase 1 of CCMI and documented in Orbe et al. (2017) (Fig.  
 157 1, red line). A more recent model version that was used in the CCMI Phase 2 simula-  
 158 tions (correspondence with Michael Manyin) is also shown (Fig. 1, green line). These  
 159 two configurations correspond to the Heracles 5.3 and Icarus 3.2 versions of the GEOS  
 160 system, respectively (Amal: I need the actual tag names).

161 We begin by comparing 10-year (2000-2010) climatological mean zonally averaged  
 162 age-of-air profiles at 50 hPa across this subset of model versions, derived from 30-year  
 163 long atmosphere-only (AMIP) integrations constrained with observed sea surface tem-  
 164 peratures (Figure 1). First, we note that the profiles for the CCMI Phase 1 version of  
 165 the model are very close to observations (black stars), consistent with the  
 166 “GEOSCCM” documented age characteristics reported in Dietmüller et al. (2018) (see  
 167 their Figure 3). In addition, while passive tracers were not integrated within MERRA-  
 168 2, results using the GEOS chemistry transport model (GEOS-CTM, Kouatchou et al.

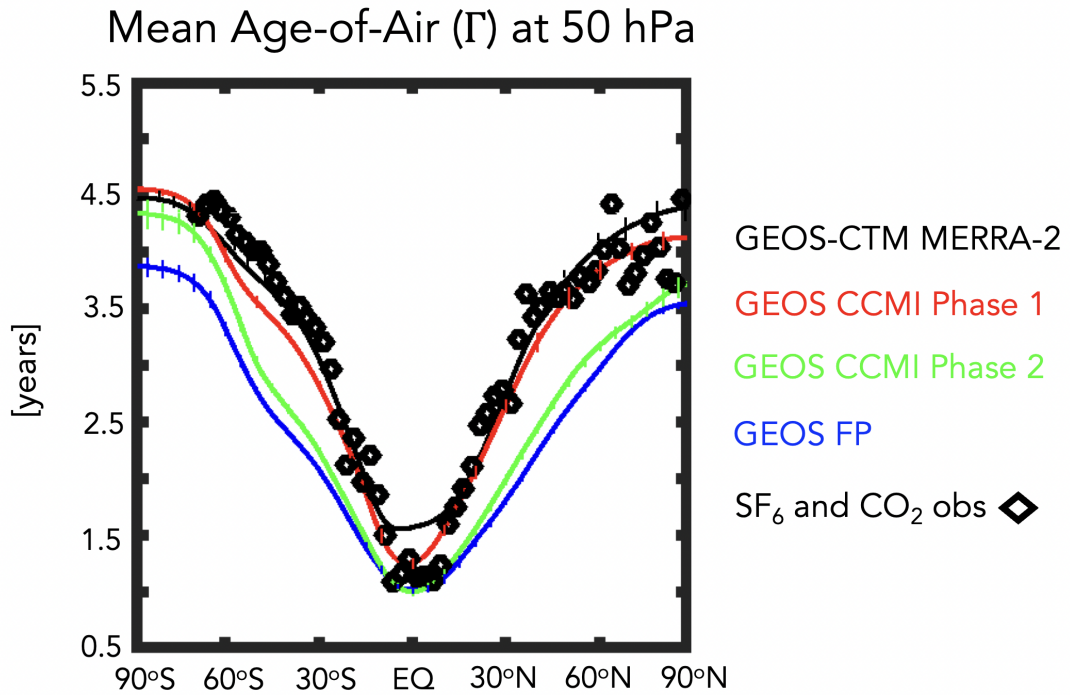


**Figure 1.** The 2000-2010 climatological annual mean meridional profile of the stratospheric mean age-of-air ( $\Gamma$ ), evaluated at 50 hPa. Results from a GEOS-CTM integration constrained with MERRA-2 meteorological fields (black line) as well as free-running GEOS simulations using a model configuration for CCMI Phase 1 (red line), CCMI Phase 2 (green line) and a more recent GEOS-FP development tag (blue line) are shown. The GEOS model versions to which these configurations correspond are the Heracles 5.3, Icarus 3.2, and Jason 3.6 tags, respectively. All simulations are constrained with the same (observed) historical sea surface temperatures. Diamonds correspond to SF<sub>6</sub> and CO<sub>2</sub> in situ based estimates of  $\Gamma$  from Boering et al. (1996) and Engel et al. (2009). Vertical dashed lines denote  $\pm\sigma$ , the standard deviation of  $\Gamma$  over 2000-2010, for each model simulation.

169 (2015)) constrained with MERRA-2 meteorological fields (black line) also exhibits good  
 170 agreement with observed values. This good agreement between the CTM-generated age-  
 171 of-air and the observations is consistent with results from a previous GEOS-CTM sim-  
 172 ulation (constrained with MERRA) that was documented in Orbe et al. (2017).

173 Moving to more recent development versions of the model (green and blue lines),  
 174 however, reveals a reduction in the mean age by  $\sim 1$  year over both southern and north-  
 175 ern high extratropical latitudes, or a decrease of  $\sim 20\text{-}30\%$  relative to MERRA-2. As dis-  
 176 cussed earlier, the green line refers to the CCM1 Phase 2 model version, whereas the blue  
 177 line refers to an undocumented candidate version (model tag Jason 3.6) that corresponds  
 178 best to a model configuration similar to what is used in the GEOS forward processing  
 179 (FP) numerical weather prediction system (Amal: As of which date?). Note that this  
 180 decrease in the age in both model versions is statistically significant, relative to inter-  
 181 nal variability (vertical bars on solid lines).

182 There are numerous development updates in the model that have occurred since  
 183 MERRA-2. Therefore, after discussing the model configurations highlighted in Figure  
 184 1 in Section 3.1, we then present results from targeted experiments aimed at successively  
 185 undoing these model updates (Section 3.2). Among those aspects most likely impact-  
 186 ing the stratospheric transport circulation, these include updates to the radiation scheme,  
 187 moving from Chou and Suarez (1994) in the shortwave and Chou (1990, 1992) in the long-  
 188 wave to the Rapid Radiative Transfer Model for GCMS (RRTGM; Iacono et al. (2008).

189 In addition to the radiation changes, another more consequential model develop-  
 190 ment was made to the handling of the remapping algorithm within the model’s FV dy-  
 191 namical core (Lin, 2004). In particular, vertical motion is realized through the Lagrangian  
 192 transport of the “floating” vertical coordinate such that after each horizontal advection  
 193 step the individual material surfaces are vertically interpolated back to standard pres-  
 194 sure levels through FV’s so-called “REMAP” algorithm. This is needed because the La-  
 195 grangian surfaces that vertically bound the finite volumes will eventually deform, neg-  
 196 atively impacting the accuracy of the horizontal-to-Lagrangian-surface transport and the  
 197 computation of the pressure-gradient terms.

198 There are various user-defined parameters and decisions that are made within the  
 199 remapping algorithm. In its current implementation this involves 1) fitting piecewise parabolic  
 200 (hereafter PPM) functions to input layer-mean values of  $T$ ,  $u$ ,  $v$ ,  $q$  and tracers; 2) cal-  
 201 culating PPM functions to output layer edges; and 3) integrating PPM functions between  
 202 output layer edges to produce new layer-mean values of  $T$ ,  $u$ ,  $v$ ,  $q$  and tracers. Note that  
 203  $T$ ,  $u$ ,  $v$ ,  $q$ ,  $C_p$ ,  $K$  and  $\Phi$  correspond to temperature, zonal wind, meridional wind, spe-  
 204 cific humidity, specific heat capacity and kinetic and potential energy, respectively. This  
 205 implementation setup is consistent with what is currently being used in most recent model  
 206 versions (i.e. blue and green lines, Figure 1) and hereafter is referred to as REMAP Op-  
 207 tion 2 (Table 1, left).

208 The alternative version – which best mimics what was used in MERRA-2 – involves  
 209 two main changes to this procedure and is hereafter referred to as REMAP Option 1 (Ta-  
 210 ble 1, right; red line in Figure 1). First steps 1) and 3) are performed only for  $u$ ,  $v$ ,  $q$  and  
 211 tracers (not  $T$ ). Second, three additional steps after 3) are added, the first two of which  
 212 involve calculating total energy (TE) at input mid-layer pressures and then performing  
 213 cubic interpolation and a posteriori integral conservation at output mid-layer pressures.  
 214 Finally, temperatures are “remapped” from total energy via  $T = (TE - K - \Phi)/C_p$ .

215 When examining Table 1, it is important to note that Options 1 and 2 differ in two  
 216 main respects. Of these, we find that the simulated ages are most sensitive to the inter-  
 217 polation that occurs within step 5 in REMAP Option 1 (Table 1). The use of TE (as  
 218 opposed to  $T$ ), by comparison, is less consequential (Appendix A, Figure A1). To this  
 219 end, the sensitivity experiments discussed in the next section mainly focus on identify-

**Table 1. Finite Volume Remapping Algorithm:** The two versions examined in this study control how individual material surfaces are vertically interpolated back to standard pressure levels. REMAP Options 2 and 1 corresponds to the configurations used in more recent (green and blue lines, Figure 1) and older (red and black lines, Figure 1) model configurations, respectively. Here  $T$ ,  $u$ ,  $v$ ,  $C_p$ ,  $K$  and  $\Phi$  correspond to temperature, zonal wind, meridional wind, specific heat of air at constant pressure and kinetic and potential energy, respectively.

Step	REMAP Option 2 (CTRL)	REMAP Option 1 (MERRA-2)
1	Fit PPM functions to input layer-mean $T$ , $u$ , $v$ , $q$ and tracers	Fit PPM functions to input layer-mean $u$ , $v$ , $q$ and tracers
2	Calculate PPM to output layer edges	Calculate PPM to output layer edges
3	Integrate PPM functions between output layer edges to produce new layer-mean $T$ , $u$ , $v$ , $q$ and tracers	Integrate PPM functions between output layer edges to produce new layer-mean $u$ , $v$ , $q$ and tracers
4	n/a	Calculate $TE = C_p T + K + \Phi$ at input mid-layer pressures
5	n/a	Calculate $TE$ at output mid-layer pressures using cubic interpolation and a-posteriori integral conservation
6	n/a	Construct “remapped” $T$ via $T = (TE - K - \Phi)/C_p$

220 ing the age sensitivities in response to changes in the interpolation scheme used in REMAP  
 221 Option 1, not to differences between the use of  $TE$  versus  $T$ .

222 Finally, it is worth noting other important model development changes that occurred  
 223 related to the parameterization of deep convection (Grell and Freitas (2014); Freitas et  
 224 al. (2018)) which could, potentially, have an indirect impact on the stratospheric circula-  
 225 tion through their influence on wave generation in the troposphere. As we show, how-  
 226 ever, while these have a substantial impacts upon their incorporation in a nonhydrostatic  
 227 version of the model on characteristics like the diurnal cycle of precipitation (Arnold et  
 228 al. (2020)) and on convective transport within the troposphere (Freitas et al. (2020)),  
 229 their indirect influence on the stratosphere is less impactful.

## 230 2.2 Model Experiments

231 In order to investigate the drivers of the differences illustrated in Figure 1 we per-  
 232 form targeted model experiments aimed at further disentangling the influence of recent  
 233 model development changes on stratospheric transport properties (Table 2). First, we  
 234 begin by defining a control experiment (CTRL; Table 2, row 1), which best corresponds  
 235 to the blue line shown in Figure 1. Then we define three new experiments based off this  
 236 control that are used to distinguish between the age changes resulting from changes in  
 237 radiation versus changes in the handling of the REMAP algorithm (Section 3.2.1).

238 Specifically, these include experiments in which we revert back from RRTMG to  
 239 Chou and Suarez (1994) in the shortwave (CSRAD; Table 2, row 2), b) revert back to  
 240 the MERRA-2 REMAP approach (i.e. REMAP Option 1) (M2REMAP; Table 2, row  
 241 3) and c) combine these two changes (CSRAD+M2REMAP; Table 2, row 4). Note that  
 242 we have also have performed experiments in which RRTMG is reverted back to Chou  
 243 (1990) in the longwave, but these changes are less impactful, compared to the shortwave  
 244 radiation changes (not shown).

**Table 2. GEOS Model Experiments:** Targeted GEOS-5 model experiments based off a control experiment (row 1) were carried out to identify the influence of radiation (row 2) and the FV remapping algorithm changes since MERRA-2 (row 3), as well as their combined influence (row 4). Sensitivities within the FV remapping algorithm were further explored with respect to the order of the interpolation scheme used to calculate TE at output mid-layer pressure levels (rows 5-7). Experiments in rows 1-4 are 30-year-long AMIPs, whereas rows 5-7 refer to 30-member 3-month-long (DJF) EMIP experiments. Both AMIPs and EMIPs are used for climate statistic evaluation (see Appendix B for more on the correspondence between the two). By comparison, rows 8-9 refer to 1-year-long DAS runs used for evaluation of the analysis state.

Experiment Name	Configuration Change	Experiment Type
CTRL	Control, REMAP Option 2	AMIP (30 yrs.)
CSRAD	Chou-Suarez (1994) Shortwave (SW) Radiation	AMIP (30 yrs.)
M2REMAP	MERRA-2 REMAP Option 1 (cubic)	AMIP (30 yrs.)
CSRAD+M2REMAP	Chou-Suarez (1994) SW + REMAP Option 1 (cubic)	AMIP (30 yrs.)
LINEAR	MERRA-2 REMAP Option 1 (linear)	EMIP (30 members)
QUADRATIC	MERRA-2 REMAP Option 1 (quadratic)	EMIP (30 members)
CUBIC	MERRA-2 REMAP Option 1 (cubic)	EMIP (30 members)
CTRL-DAS	Control, REMAP Option 2	DAS (1 yr.)
CUBIC-DAS	MERRA-2 REMAP Option 1 (cubic)	DAS (1 yr.)

245 As shown in Section 3.2.1, the M2REMAP experiment produces the largest changes  
 246 in age-of-air, compared to the altered radiation experiments. To this end, we focus the  
 247 remainder of our investigation (Section 3.2.2) on examining a clean set of experiments  
 248 that distinguishes the impact of REMAP Option 1 versus Option 2 on simulated trans-  
 249 port. In particular, we perform three sensitivity experiments that differ from each other  
 250 only in terms of the calculation of TE at the mid-layer pressure levels, which we perform  
 251 using a linear (LINEAR; Table 2, row 5), quadratic (QUADRATIC; Table 2, row 6) and  
 252 cubic interpolation (CUBIC; Table 2, row 7) scheme, with the latter corresponding to  
 253 the approach that was used in MERRA-2. Note that, while the LINEAR and QUADRATIC  
 254 experiments do not actually correspond to any of the development tags shown in Fig-  
 255 ure 1, they highlight the large sensitivity of the mean age to changes in the interpola-  
 256 tion scheme that may otherwise seem innocuous. They also provide further evidence of  
 257 the strong influence of tropical lower stratospheric upwelling strength on stratospheric  
 258 mean age in GEOS.

259 Finally, in all experiments using REMAP Option 1 (i.e. M2REMAP, CSRAD+  
 260 M2REMAP, LINEAR, QUADRATIC, CUBIC) additional modifications to the diver-  
 261 gence damping coefficients were used so as to best ensure consistency with what was used  
 262 in MERRA-2. Specifically, these include changes to the number of layers for vertical sub-  
 263 grid mixing, the DAS coefficient for barotropic mode damping, the use of 2<sup>nd</sup> vs. 6<sup>th</sup> or-  
 264 der divergence damping and the strength of the divergence damping coefficients.

## 265 2.3 Analysis Approach

### 266 2.3.1 Stratospheric Circulation and Transport Diagnostics

267 To diagnose the transport circulation we focus primarily on the age-of-air (Hall and  
 268 Plumb (1994)). This is inferred from an idealized global “clock” or ideal age tracer ( $\Gamma$ )



(Thiele and Sarmiento (1990)) that is defined with respect to all grid points in the first model level. Initially, the ideal age tracer is set to zero throughout the troposphere and thereafter held to zero over the entire Earth’s surface, subject to a constant aging of 1 year/year throughout the atmosphere. We present here the statistically stationary (equilibrated) value of  $\Gamma(r)$ , which is equal to the average time since the air at a location  $r$  in the stratosphere last contacted the Earth’s surface. In addition to the mean age, we also show results from an idealized e90 tracer that is uniformly emitted over the entire surface layer and decays exponentially at a rate of 90 days<sup>-1</sup> such that concentrations greater than 125 ppb and less than 50 ppb tend to reside in the lower troposphere and stratosphere, respectively (Prather et al. (2011)). As this tracer features strong near-tropopause gradients and takes significantly less time to equilibrate, compared to the mean age, it is useful for evaluating stratosphere-troposphere-exchange and transport within the upper troposphere/lower stratosphere (Abalos et al. (2017, 2020); Orbe et al. (2020)).

In addition to the idealized tracers, we also evaluate the impacts of the age changes on real trace gas distributions. Two of the experiments shown here were run with full interactive chemistry and correspond to the two CCM1 (Phase 1 and Phase 2) integrations (red and green lines, Figure 1), which both employed the same Global Modeling Initiative (GMI) chemical mechanism (Strahan et al. (2013)). Results from these experiments show the imprint of the age-of-air changes on nitrous oxide (N<sub>2</sub>O) and methane (CH<sub>4</sub>).

As we show in Section 3, the changes in age-of-air across the different model versions are strongly tethered to changes in the advective component of the circulation, which we quantify using the Transformed Eulerian Mean (TEM) estimate of the Lagrangian transport of mass by the circulation. Thus, in addition to more standard Eulerian metrics of the circulation (e.g., zonal winds and temperatures), we focus on the vertical component of the TEM residual velocity, defined as  $\bar{w}^* = \bar{w} + \frac{\partial(\psi \cos \phi)}{\partial \phi}$ , where  $\psi = \bar{v}'\theta' / \frac{\partial \theta}{\partial p}$  is the eddy stream function,  $\theta$  refers to potential temperature and overbars and primes denote zonal means and deviations therefrom, respectively (Andrews et al. (1987)). In addition, we interpret the behavior in  $w^*$  using the Eliassen-Palm flux divergence ( $\nabla \cdot \mathbf{F}$ ), whose horizontal ( $\mathbf{F}(\phi)$ ) and vertical ( $\mathbf{F}(p)$ ) components are respectively defined as  $\mathbf{F}(\phi) = \cos \phi [\frac{\partial u}{\partial p} \psi - \bar{u}'v']$  and  $\mathbf{F}(p) = \cos \phi ([f - \frac{\partial u \cos \phi}{\partial \phi}] \psi - \bar{u}'\omega')$ .

### 2.3.2 Experimental Setup

We begin our analysis by interpreting the results shown in Figure 1, which are all based on historical AMIPs that were performed at the same cubed sphere C180 (approximately half-degree) horizontal resolution. As they represent more “official” model versions they serve as an important motivation for the experiments that follow. However, a clean/meaningful analysis of this set of runs is nonetheless hampered by the structural model differences between them.

Given the limitations of the experiments highlighted in Figure 1, we focus the bulk of our analysis on the model configurations listed in Table 2. For a subset of these model runs (rows 1-4) climatological AMIPs were carried at a C180 resolution and used to infer the climate characteristics of the different model configurations. For the other experiments (Table 2, rows 5-7) so-called “EMIPs” – ensembles of 3-month-long integrations initialized on approximately November 15 of each year between 1985 and 2015 – were performed. EMIPs for these experiments were performed at both C180 and C360 resolutions in order to examine the sensitivity of our results to changes in horizontal resolution. All of the experiments listed in Table 2 were integrated using the same idealized passive tracer package (including the e90 and  $\Gamma$  tracers) described in Orbe et al. (2017).

As shown in Appendix B, comparisons of the the December-January-February (DJF) vertical profile of  $w^*$ , averaged over 1985-2015 and between the tropical turnaround lat-

itudes, show excellent agreement between EMIP and AMIP integrations carried out using the same model configuration (Appendix Figure B1). This somewhat incidental result, represents, to the best of our knowledge, the first time that EMIP-based statistics have been shown to converge well to those from AMIPs for the stratospheric metrics considered in this study. This suggests that EMIPs may provide a computationally more efficient alternative to AMIPs for use in quickly ascertaining the impacts of model changes. We note, however, that this approach is not appropriate for evaluating the time-integrated transport characteristics reflected in the age-of-air. To this end, we show results from both AMIP and EMIP experiments.

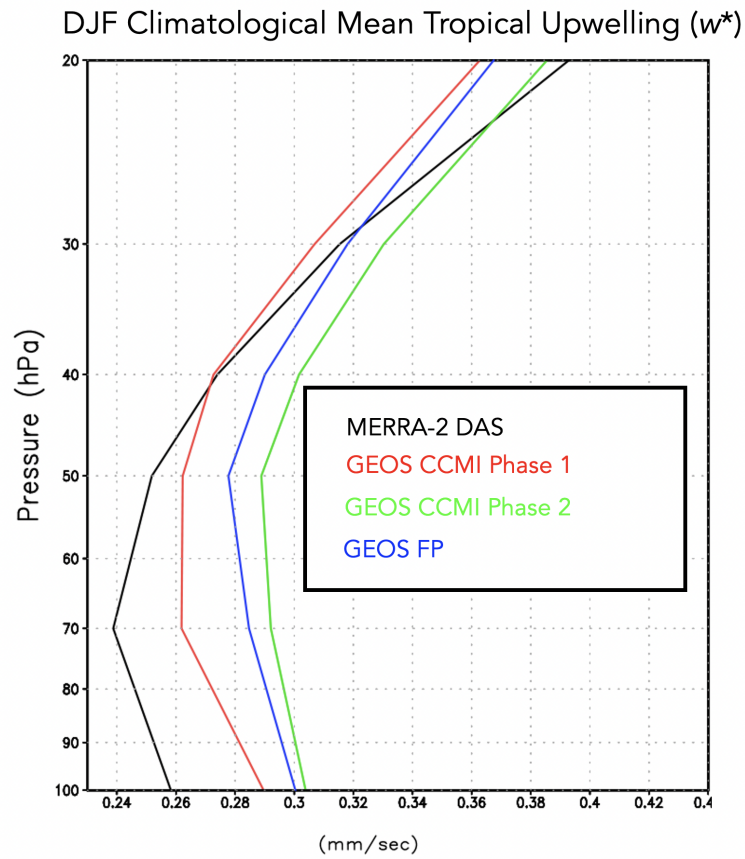
Finally, in addition to examining the climate statistics of the different model configurations we also inquire into implications for the analyzed atmospheric states from data assimilation for a subset of the experiments (Table 2, rows 8-9). Specifically, we examine the root-mean-square error of various climate fields (*Amal, need description of relevant metrics/analysis*). This evaluation is important given that in GEOS-R21C any underlying model biases will be partly ameliorated through replaying of the model state to the analysis. Assessing the impact of reduced biases from the free-running model for the analysis state is therefore important for informing the development of GEOS-R21C.

## 2.4 Observations and Reanalyses

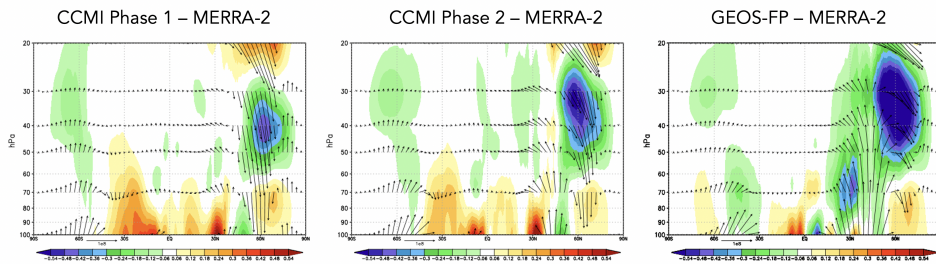
While our focus is on interpreting and understanding the different model configurations, we incorporate observations to provide context when possible, although we do not present an exhaustive evaluation of the model’s transport characteristics (for that see earlier studies including Orbe et al. (2017, 2018)). However, as the tracers are not directly integrated in MERRA-2 (with the exception of ozone), we compare against independent observational estimates. For the mean age we first compare simulated meridional age profiles at 50 hPa with values derived from in situ aircraft measurements of carbon dioxide (CO<sub>2</sub>), averaged in 2.5 degree latitude bins over the altitude range 19.5 to 21.5 km (Boering et al. (1996), see also Figure 5 in Hall et al. (1999)).

We also briefly evaluate impacts of transport biases on the simulated trace gas distributions for the CCM1 Phase 1 and 2 experiments. The simulated fields of methane (CH<sub>4</sub>) are compared with the climatologies derived for 1991–2002 from the Halogen Occultation Experiment (HALOE) on board the Upper Atmosphere Research Satellite (UARS) (Groß and Russell III (2005)). Comparisons of simulated nitrous oxide (N<sub>2</sub>O) are made against 2005–2015 climatologies derived from the Microwave Limb Sounder (MLS) on the Earth Observing System (EOS) Aura satellite. We use the 190-GHz retrieval from Version 4.2 because the 640-GHz data set ends in summer 2013 due to the failure of the N<sub>2</sub>O primary band.

For the circulation diagnostics nearly all comparisons are made relative to MERRA-2 and comparisons against ERA-5 (not shown) reveal a similar picture. There is one exception, however, as special care must be taken when evaluating the (highly derived) TEM circulation. In particular, calculations of the TEM circulation are notoriously sensitive not only to differences in the formulation of the equations (Hardiman et al., 2010), but also to the vertical resolution of the input velocities and associated heat and momentum fluxes that are used to calculate the vertical derivatives in the eddy stream function and EP flux components (Gerber & Manzini, 2016). In this respect, it is essential that comparisons of the simulated TEM circulation must be made using consistent calculations. For the case of the AMIPs shown in Figure 1 and for the targeted experiments listed in Table 2 this is ensured by the use of an identical output vertical grid (consisting of ? levels, *Larry, need number of vertical levels in CSRAD, etc. experiment output*). However, comparisons with MERRA-2 are complicated as that data is only available at a lower output vertical resolution (? levels, *Larry, how many model output levels are used for calculating  $w^*$  in MERRA2?*). This results in spurious differences in the vertical struc-



**Figure 2.** The DJF 1985-1994 climatological mean vertical residual mean velocity,  $w^*$ , averaged between the turnaround latitudes for GEOS model configurations corresponding to the CCMI Phase 1 (red) and Phase 2 (green) submissions and to GEOS-FP (blue). M2AMIP is shown in black. **Replace MERRA-2 black line with M2AMIP.**

DJF Climatological Mean Eliassen-Palm Flux Divergence ( $\nabla \cdot F$ )

**Figure 3.** Colors show anomalies in the DJF climatological mean Eliassen-Palm (EP) flux divergence between the CCMI Phase 1 (left), CCMI Phase 2 (middle) and GEOS-FP (right) model versions, relative to MERRA-2. Arrows denote anomalies in the vertical and meridional EP flux vectors (relative to MERRA-2). **Replace MERRA-2 with M2AMIP.**

370 ture of the TEM circulation with MERRA-2 that are not physically driven. To this end,  
 371 when comparing the TEM circulation in the A(E)MIPS, in lieu of MERRA-2 we use re-  
 372 sults from a 30-member AMIP ensemble that was performed using the MERRA-2 sys-  
 373 tem (hereafter M2AMIP) and for which we have output on the higher resolution out-  
 374 put grid. This ensures an apples-to-apples comparison of the TEM in the various GEOS  
 375 experiments with the MERRA-2 system as possible (note that for non-derived measures  
 376 (i.e. winds, temperatures) the raw MERRA-2 output is used). **Larry/Kris/Amal: Is there**  
 377 **a reference for the M2AMIP ensemble?.**

### 378 3 Results

#### 379 3.1 Reduction in Stratospheric Mean Age Since MERRA-2

380 We begin by interpreting the reduction in mean age exhibited in more recent model  
 381 versions in terms of changes in the strength of upwelling in the tropical lower stratosphere.  
 382 In particular, the reductions in  $\Gamma$  (Figure 1) are consistent with increases in the strength  
 383 of lower stratospheric tropical upwelling, with  $w^*$  becoming progressively stronger in more  
 384 recent model tags, relative to MERRA-2 (Figure 2). Though perhaps naive, this rela-  
 385 tionship between lower stratospheric upwelling and the mean age is consistent with the  
 386 long-term behavior of  $\Gamma$  inferred from both historical and projected future climate sim-  
 387 ulations (Butchart et al. (2010); Abalos et al. (2021)). A strong relationship between the  
 388 strength of lower stratospheric ascent and the mean age was also shown to hold in the  
 389 CCMVal models (see Fig. 5.20 in J. Neu et al. (2010)). Nevertheless, it is important to  
 390 note that a clear relationship between  $w^*$  and  $\Gamma$  is not a priori expected, as the age-of-  
 391 air is also known to be very sensitive to mixing, which may be important in interpret-  
 392 ing differences among the CCMI Phase 1 models (Dietmüller et al. (2018)).

393 The differences in  $w^*$  highlighted in Figure 2 are associated with enhanced Eliassen-  
 394 Palm flux convergence over NH midlatitudes (Figure 3). Increased wave convergence is  
 395 evident not only within the subtropical lower stratosphere ( $< 30^\circ\text{N}$ , 50-100 hPa) but also  
 396 over higher latitudes and altitudes ( $\sim 40^\circ\text{-}70^\circ\text{N}$ , 20-50 hPa). The fact that differences  
 397 in extratropical wave convergence imprint on tropical upwelling is consistent with our  
 398 understanding of the so-called “downward control” principal (Haynes et al. (1991)). In  
 399 particular, the strength of the residual mean streamfunction ( $\Psi^*$ ) is, via downward  
 400 control, directly related to the vertically integrated eddy-induced total zonal force above that  
 401 level and has contributions both from the (resolved wave) Eliassen-Palm flux divergence

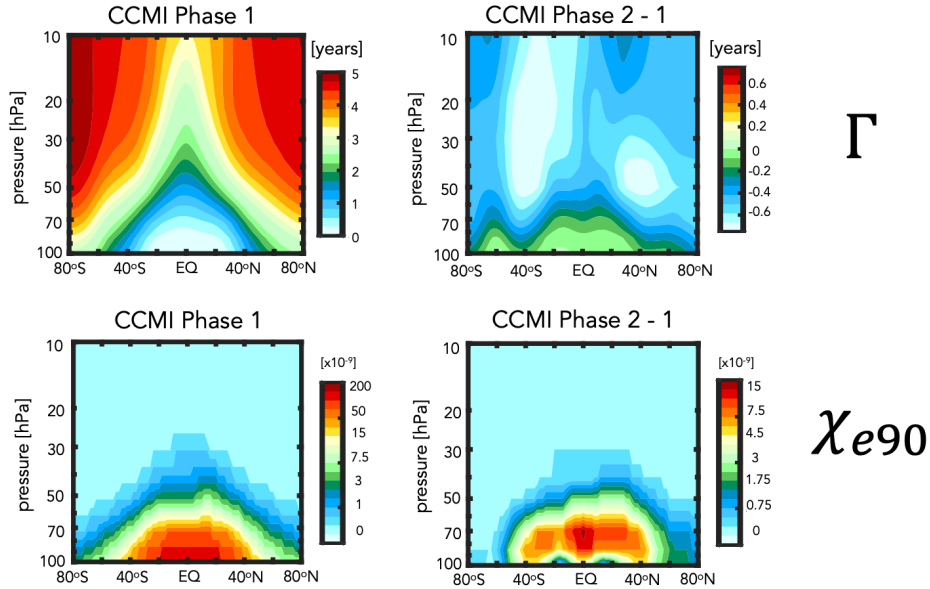


**Figure 4.** The climatological mean (2000-2010) distribution of the mean age-of-air ( $\Gamma$ ) (left, top) and e90 idealized tracers (left, bottom) for the CCMI Phase 1 model configuration. Climatological differences between the CCMI Phase 2 and Phase 1 model configurations are shown in the left panels. Note that a nonlinear colorbar has been used in the e90 subplots.

402 (Figure 3) as well as parameterized waves (not shown). The tropical upward mass flux  
 403 – defined as  $\Psi_{\max}^* - \Psi_{\min}^*$  evaluated at the turnaround latitudes (e.g. Rosenlof (1995)) –  
 404 is therefore directly dependent on the wave forcing aloft.

405 While the reduction in  $\Gamma$  (Figure 1) of  $\sim 30\%$  at 50 hPa is significant, it is neither  
 406 clear if this change is representative of other altitudes within the stratosphere nor how  
 407 this age bias imprints on real chemical species. To this end, we begin by comparing the  
 408 full latitude-pressure distribution of changes in  $\Gamma$  and another passive tracer (e90) (Fig-  
 409 ure 4) between the CCMI Phase 1 and Phase 2 model configurations (red and green lines,  
 410 Figure 1). In particular, we find that the changes in both passive tracers – large reduc-  
 411 tions in  $\Gamma$  within both hemispheres (Fig. 4, top right) and increased values of e90 within  
 412 the lower stratosphere (Fig. 4, bottom right) – are reflective of an overall increase in the  
 413 strength of the transport circulation. This is highlighted in the CCMI Phase 2 – 1 model  
 414 differences for the passive tracer distributions (Fig. 4, right panels) which are shown in  
 415 the absence of robust observational constraints of  $\Gamma$  at higher altitudes (or any obser-  
 416 vational constraints for e90, for that matter). The reduced/increased stratospheric bur-  
 417 dens of the age and e90 tracers are consistent with stronger upwelling in the CCMI Phase  
 418 2 model configuration (Figure 2).

419 While the observational constraints on  $\Gamma$  presented in Figure 1 and the departure  
 420 of  $w^*$  away from MERRA-2 suggest that transport properties of the newer model con-  
 421 figurations are moving in the wrong direction, it is relevant to ask whether or not the  
 422 trace gas satellite measurements also support this conclusion. Indeed, comparisons with  
 423 observations show larger biases in  $\text{N}_2\text{O}$  (Fig. 5, top panels) and  $\text{CH}_4$  (Fig. 5, bottom pan-  
 424 els), increasing from 10% to 30% in the CCMI Phase 2 model configuration, depending  
 425 on the species. The patterns of these biases are generally consistent with the biases in

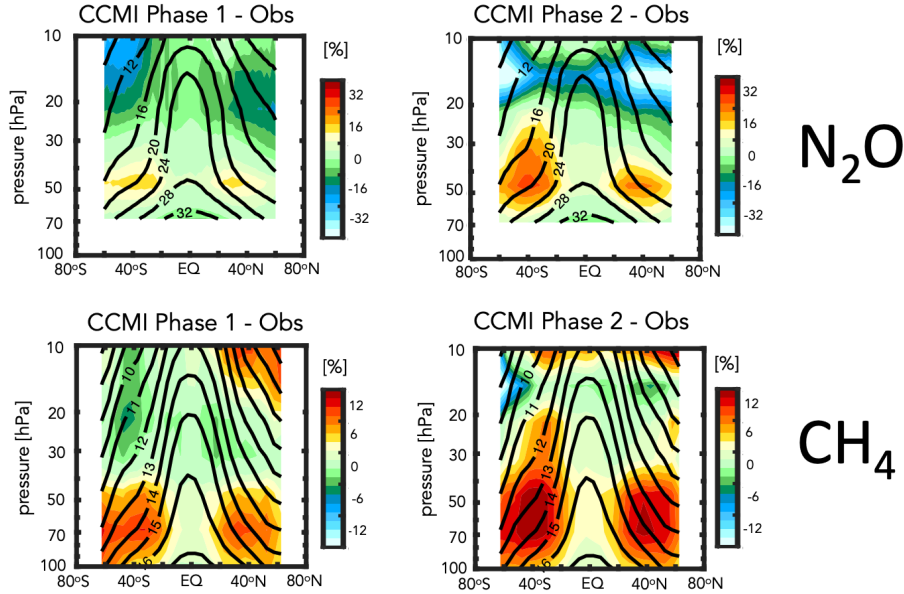


**Figure 5.** Colors shown anomalies in the simulated distributions of nitrous oxide ( $N_2O$ ) (top) and methane ( $CH_4$ ) (bottom), relative to the MLS and HALOE observed values, respectively, for the CCMI Phase 1 (left) and Phase 2 (right) GEOS model configurations. Climatological mean observed values are shown in the black contours.

the mean age (Fig. 4), suggesting a strong link between the tracers. Recall that the same chemistry mechanism is used in both CCMI Phase 1 and 2 simulations.

The fact that the mean age changes have a significant imprint on the simulated trace gases is consequential for the GEOS-RC21 system. However, the configurations shown in Fig. 1-5 differ in many respects (physics, resolution, radiation, FV remapping algorithm) and it is difficult to meaningfully interpret what is driving the changes in  $w^*$  (and the tracers). We therefore move next to the targeted model experiments (Table 2) in order to interpret the model development steps that resulted in these transport circulation changes.

### 3.2 Identifying Drivers of Upwelling and Tracer Changes Since MERRA-2

#### 3.2.1 Radiation versus REMAP Algorithm

As discussed in Section 2, among the model changes that were made since MERRA-2, the changes in radiation and the FV remapping algorithm are most likely to directly have impacted the stratospheric circulation. We therefore begin by assessing which of these changes dominates the decreases in  $\Gamma$  shown in Figure 1.

Figure 6 shows the distribution of  $\Gamma$  for experiments in which the shortwave radiation and REMAP updates since MERRA-2 have successively been undone. Relative to the control experiment (CTRL; Table 2, row 1), the reversion back to Chou (1992) in the shortwave results in an increase in the mean age of  $\sim 0.5$  years throughout the stratosphere (CSRAD; Table 2, row 2). Though significant, this change in  $\Gamma$  is smaller than the change that results from reverting back to REMAP Option 1 (M2REMAP; Table 1; row 3), in which the mean age increases by  $\sim 1$  year. The combined impacts of both

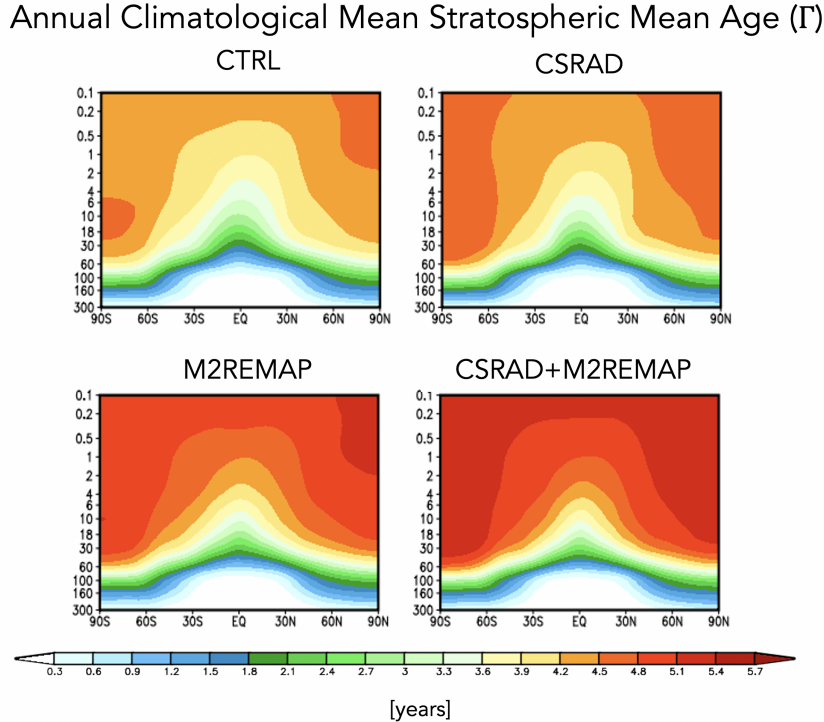


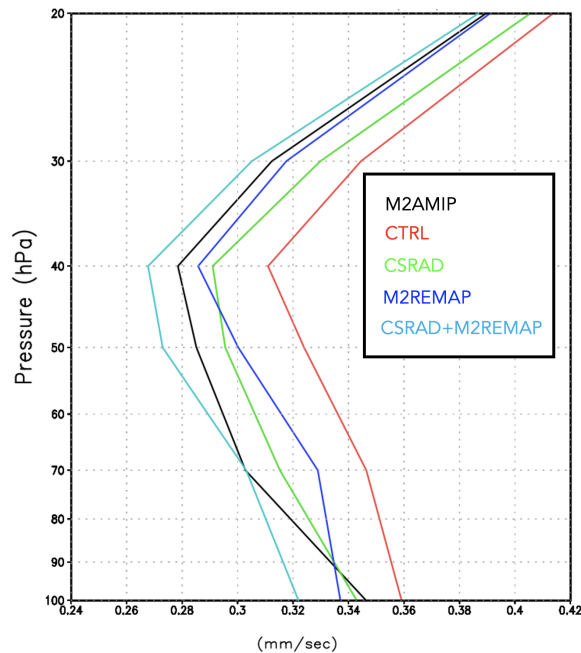
**Figure 6.** Colors show the simulated 2000-2010 climatological annual mean distributions of the mean age-of-air ( $\Gamma$ ) for the CTRL (top left; Table 1, row 1), CSRAD (top right; Table 1, row 2), M2REMAP (bottom left; Table 1, row 3) and combined CSRAD+M2REMAP (bottom right; Table 1, row 4) experiments.

449 changes (CSRAD+M2REMAP; Table 1 row 4) is roughly linear, with age values of  $\sim$   
 450 5.5 years over high latitudes at 50 hPa, consistent with the values simulated by the GEOS-  
 451 CTM MERRA-2 integration (black line, Figure 1) and with the CCM1 Phase-1 version  
 452 of the model (red line, Figure 1).

453 Next we ask if the behavior of  $\Gamma$  exhibited in Figure 6 can be interpreted in terms  
 454 of changes in the strength of lower stratospheric tropical upwelling and extratropical wave  
 455 convergence, as our previous analysis of the CCM1 experiments suggested. Indeed, Figure  
 456 7 shows that values of upwelling decrease in the CSRAD and M2REMAP experiments,  
 457 relative to the CTRL integration. The increase in upwelling resulting from both changes  
 458 (CSRAD+M2REMAP) is still larger, consistent with the larger age decreases in that exper-  
 459 iment. This change in the behavior of  $w^*$  within the tropical stratosphere can be inter-  
 460 preted in terms of changes in the Eliassen Palm flux convergence over NH midlati-  
 461 tudes (not shown), which features smaller values in the CSRAD, M2REMAP (and CSRAD+  
 462 noindentMSREMAP) experiments. Note that our examination of the changes in  
 463  $w^*$  are derived from EMIP integrations, which we showed previously converge (for DJF)  
 464 to the statistics derived from corresponding AMIP experiments.

### 465 **3.2.2 FV REMAP Algorithm: Sensitivity of Climate Statistics**

466 Having shown in the previous section that the largest changes in the mean age were  
 467 realized through the reversion back to REMAP Option 1, we now investigate further the  
 468 sensitivity of the transport circulation to the choice of remapping interpolation scheme.  
 469 In particular, we compare simulations in which total energy is calculated at new mid-

DJF Climatological Mean Tropical Upwelling ( $w^*$ )

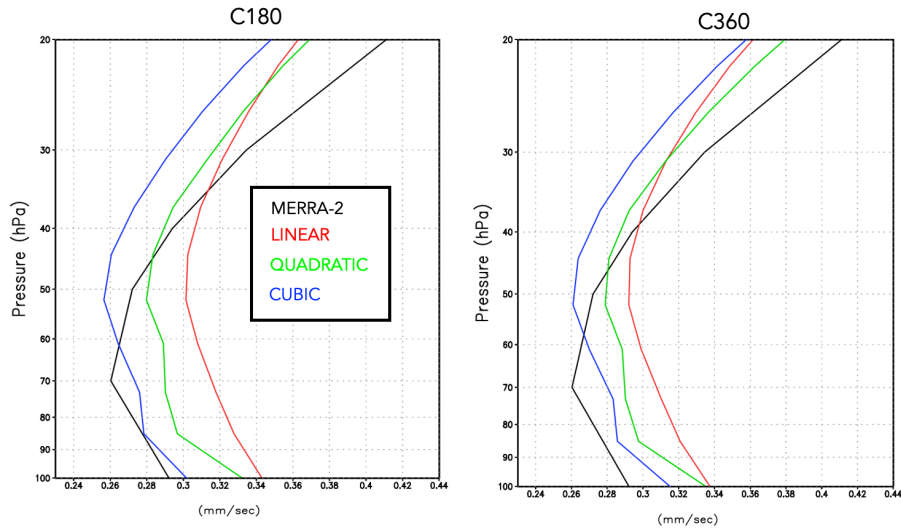
**Figure 7.** The DJF climatological mean vertical residual mean velocity,  $w^*$ , averaged between the turnaround latitudes for the CTRL (red line; Table 2, row 1), CSRAD (green line; Table 2, row 2), M2REMAP (blue line; Table 2, row 3) and combined CSRAD+M2REMAP (cyan line; Table 2, row 4) experiments. M2AMIP is shown in black.

470 layer pressures using cubic, quadratic and linear interpolation prior to the aposterior in-  
 471 tegral conservation (Table 2, rows 5-7). In addition, in this section we seek to understand  
 472 how the changes in the Eliassen-Palm flux convergence over NH midlatitudes arise via  
 473 analysis of the large-scale wind structure.

474 Figure 8 (left panels) shows a clear sensitivity in tropical upwelling to the choice  
 475 of interpolation scheme, with  $w^*$  progressively increasing in strength moving from the  
 476 CUBIC to QUADRATIC to LINEAR schemes. This sensitivity is robust across horizon-  
 477 tal resolutions as the same suite of experiments performed at C360 exhibit the same sensi-  
 478 tivity (Fig. 8, right panels). While no current model tag actually employs a linear scheme,  
 479 this suite of experiments highlights the strong sensitivity to choice of interpolation scheme  
 480 within the remapping algorithm; to the best of our knowledge, this result has not been  
 481 reported in the literature. Furthermore, as we show next, this clean set of experiments  
 482 allow us to inquire mechanistically into the processes that are driving the changes in wave  
 483 convergence over midlatitudes, unencumbered by differences in horizontal resolution, physics,  
 484 etc.

485 Consistent with our expectations based on the analysis of the previous experiments,  
 486 the drivers of the changes in  $w^*$  are related to increased wave convergence moving from  
 487 the CUBIC to QUADRATIC to LINEAR schemes (Figure 9). Over extratropical lat-  
 488 itudes, the zonal force associated with this enhanced wave convergence is associated with  
 489 enhanced downwelling at high latitudes that, through mass balance, is accompanied by  
 490 enhanced upwelling in the tropics. This indirect impact of higher latitude wave drag is  
 491 evident in Appendix Figure C1, which show stronger upwelling/downwelling in LINEAR  
 492 and QUADRATIC experiments over the tropics/polar region.



DJF Climatological Mean Upwelling ( $w^*$ )

**Figure 8.** The DJF climatological mean vertical residual mean velocity,  $w^*$ , averaged between the turnaround latitudes for the CTRL (cyan line; Table 2, row 1), LINEAR (green line; Table 2, row 5), and QUADRATIC (blue line; Table 2, row 6) experiments. MERRA-2 is shown in black. **Replace MERRA-2 with M2AMIP.**

493 Next we exploit the fact that these experiments only differ with respect to the in-  
 494 terpolation scheme in order inquire further into the drivers of the wave convergence changes.  
 495 To this end, Figure 10 compares profiles of the zonal mean zonal wind between the CU-  
 496 BIC, QUADRATIC and LINEAR experiments, averaged over the region of enhanced wave  
 497 convergence (i.e. 20°N-60°N). The experiments featuring stronger wave convergence (LIN-  
 498 EAR and QUADRATIC) are also simulations with stronger zonal winds, relative to MERRA-  
 499 2, especially above 70 hPa. This change in winds occurs at both C180 (Fig. 10, left panel)  
 500 and C360 (Fig. 10, right panel) resolutions.

501 Structurally, the increase in zonal wind strength over northern extratropical mid-  
 502 latitudes is reflective of a poleward shift in the zonal winds as the critical latitude, i.e.  
 503 where the zonal wind is zero, shifts northward in the QUADRATIC and, especially, LIN-  
 504 EAR integrations, relative to the CUBIC experiment (Figure 11). Since stationary waves  
 505 only propagate in westerly zonal flow, the latitude where zonal flow is zero acts a bound-  
 506 ary for wave propagation (Hardiman et al. (2014)). As a result, this shift in critical lat-  
 507 itude results in enhanced wave propagation in that region.

508 Figures 10 and 11 highlight how the changes in zonal winds in the LINEAR and  
 509 QUADRATIC experiments reflect a degradation in model skill, relative to MERRA-2,  
 510 throughout the entire stratosphere. The changes in upwelling, mean age, chemical trace  
 511 gases and zonal winds thus provide a coherent and self-consistent picture suggestive of  
 512 a degradation in the representation of the stratospheric circulation since MERRA-2. That  
 513 is, an increased bias in the stratospheric northern zonal winds are, via their influence on  
 514 wave convergence, compromising changes in the strength of the mean meridional over-  
 515 turning circulation and its impact on composition. It is interesting to note that the wind  
 516 biases also extend into the troposphere and show degraded skill relative to MERRA-2  
 517 in the LINEAR and QUADRATIC experiments (Figure 11). Examination of other fields  
 518 (i.e. tropopause biases, Appendix Figure D1) present somewhat more of a nuanced story

## DJF Climatological Mean Eliassen-Palm Flux Divergence ( $\nabla \cdot \mathbf{F}$ )

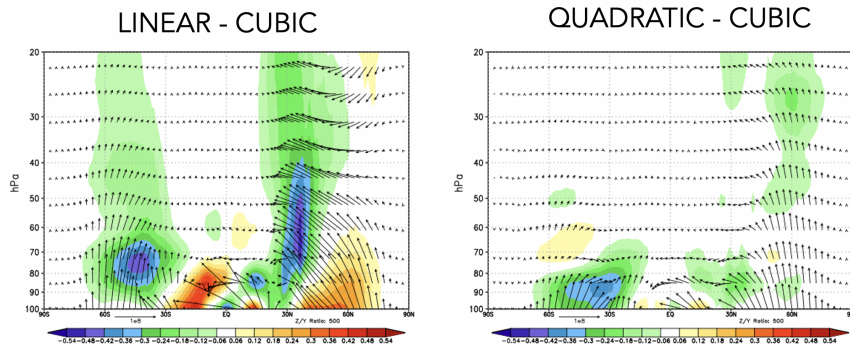


**Figure 9.** Colors shown anomalies in the DJF climatological mean Eliassen-Palm (EP) flux divergence in the LINEAR (left) and QUADRATIC (right) experiments, relative to the CUBIC model experiment. Arrows denote anomalies in the vertical and meridional EP flux vectors.

## DJF Climatological Mean Zonal Wind (20°N-60°N)

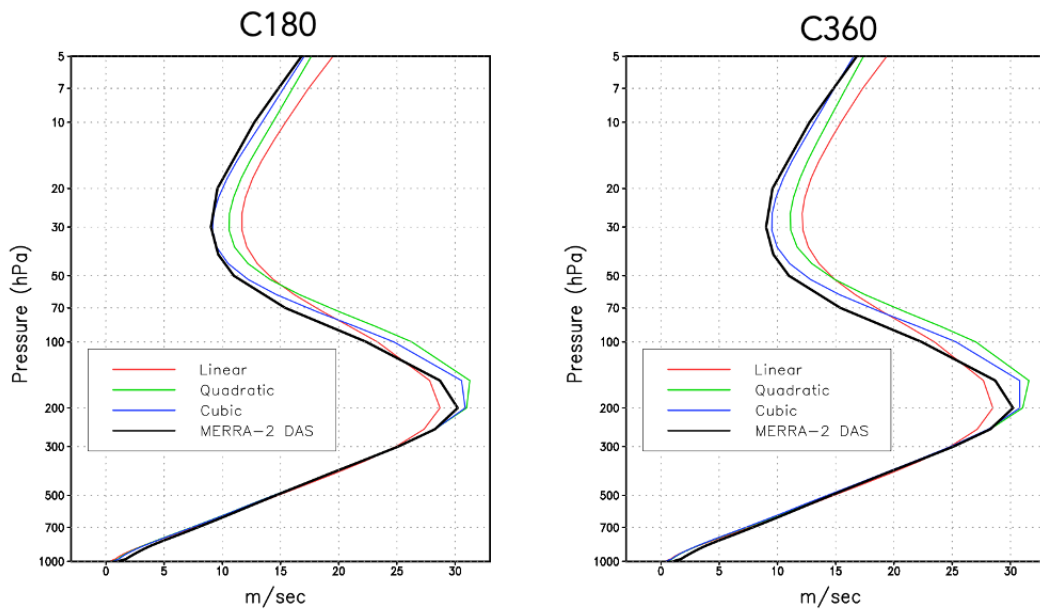


**Figure 10.** Vertical profiles of the DJF climatological mean zonal mean zonal winds in the LINEAR (red), QUADRATIC (green) and CUBIC (blue) experiments, averaged between 20°N and 40°N. MERRA-2 is shown in the black line. Results for both C180 (left) and C360 (right) experiments are provided.

## DJF Climatological Zonal Mean Zonal Wind Anomalies Relative to MERRA-2

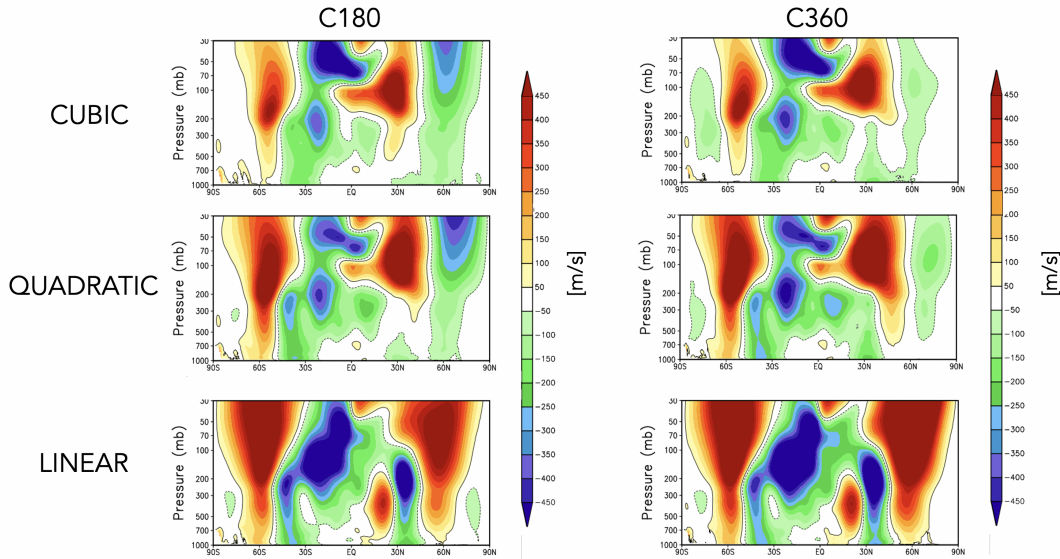


**Figure 11.** Colors shown anomalies in the DJF climatological mean zonal mean zonal winds in the CUBIC (top), QUADRATIC (middle) and LINEAR (bottom) experiments, relative to MERRA-2. Results for both C180 (left) and C360 (right) experiments are provided.

519 that depends more sensitively on latitude and season considered. The improvements in  
 520 the zonal winds, however, are most relevant for setting the upwelling characteristics within  
 521 the tropical lower stratosphere via their influence on wave propagation into that region.

522 Finally, to better understand why these impacts on the winds have such a conse-  
 523 quence for the wave convergence properties within the stratosphere, next we examine the  
 524 zonal structure of these biases in the middle stratosphere (Figure 12). This reveals that  
 525 the enhanced winds in the LINEAR (and, to a lesser extent, QUADRATIC) integrations  
 526 are concentrated over the North Pacific at both C180 (Fig. 12, left) and C360 (Fig. 12,  
 527 right) resolutions (a similar picture emerges within the troposphere, not shown). As this  
 528 region is the primary region dominating the stationary component of the upward flux  
 529 of vertical wave activity (Plumb (1985), see their Figure 4) it is perhaps not surprising  
 530 that this region is having a profound impact on the mean overturning circulation. Again,  
 531 as with the zonal mean wind changes, the increases in wind strength over the North Pa-  
 532 cific represent degraded model skill relative to MERRA-2. Note that comparisons with  
 533 ERA-5 reveal a similar bias (not shown).

### 534 3.2.3 FV REMAP Algorithm: Sensitivity of DAS Analysis State

535 Up to this point our focus has been on evaluating the various model configurations  
 536 via use of 30-year long AMIPs, which are required for deriving the integrated transport  
 537 statistics (i.e. age-of-air) that reflect the long timescales relevant to setting the strato-  
 538 spheric transport circulation. However, this not only poses practical challenges for model  
 539 development purposes (which may be ameliorated, for some variables, through use of EMIPs),  
 540 but it is also not obvious how the time-integrated model biases inferred from AMIPs man-  
 541 ifest in a data assimilation (DAS) context. To this end, here we briefly comment on im-  
 542 plications for the DAS analysis state.

### DJF Climatological 30 hPa Zonal Wind Anomalies Relative to MERRA-2

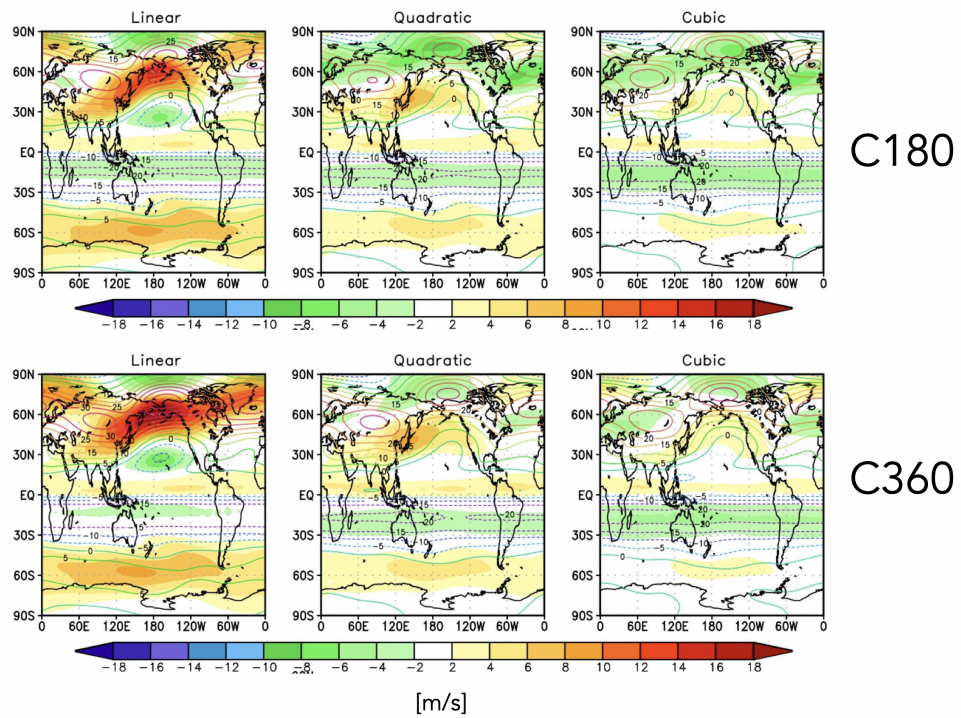


**Figure 12.** Colors shown anomalies in the DJF climatological mean zonal winds at 30 hPa in the CUBIC (right), QUADRATIC (middle) and LINEAR (left) experiments, relative to MERRA-2. Results for both C180 (top) and C360 (bottom) experiments are provided.

## PLACEHOLDER

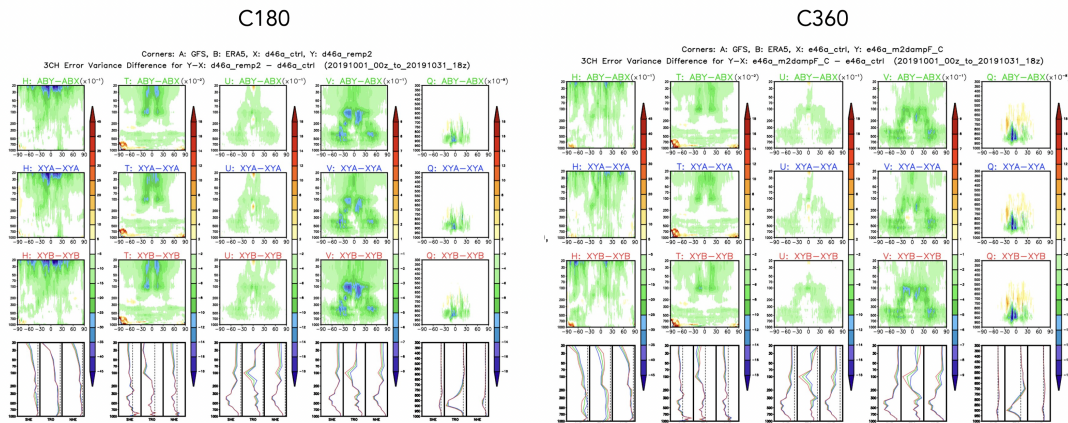


**Figure 13.** Need to fill in when figure has been decided.

543 In particular, we compare two DAS experiments one mimicking MERRA2 (d46aremp2)  
 544 and one mimicking the control configuration (d46actrl) (Table 2, rows 8-9). As in the  
 545 previous section, we also consider the robustness of results to changes in horizontal res-  
 546 olution.

547 *Need to write when receive Amal's new figure (current Figure 13 is only a place-*  
 548 *holder).*

#### 549 4 Conclusions

550 Here we have presented an analysis aimed at understanding differences in the rep-  
 551 resentation of the stratospheric circulation in recent candidate systems for GEOS-R21C,  
 552 relative to older versions of GEOS-5 similar to that which was used to produce MERRA-  
 553 2. Using targeted model experiments oriented at disentangling various model develop-  
 554 ment updates, we have identified a key role played by changes in the remapping algo-  
 555 rithm within the model's finite-volume dynamical core. Our key results are as follows:

556 #1. The stratospheric mean age-of-air in GEOS-5 is sensitive to the degree of the  
 557 interpolation scheme that is used to calculate layer-mean values of total energy,  $u$ ,  $v$  and  
 558 tracers. Different treatment of the vertical remapping algorithm (REMAP Option 1 vs.  
 559 2) result in mid-stratospheric (50 hPa) age-of-air differences of  $\sim 1$  year over high lat-  
 560 itudes, or about 30% climatological mean values.

561 #2. The age-of-air sensitivities reflect, to first order, changes in the strength of trop-  
 562 ical upwelling associated with the Brewer-Dobson circulation which are in turn are driven  
 563 by changes in EP flux convergence over northern midlatitudes. Changes in wave conver-  
 564 gence reflect shifts in (critical lines of) wave propagation that originate in the troposphere  
 565 over the Pacific Ocean, a region of strong upward wave activity.

566 #3. The degradation of age-of-air, upwelling and zonal wind climate statistics man-  
 567 ifest in AMIPs, also translate to degradations in the DAS analysis states of a broad range  
 568 of variables. These results are are not sensitive to horizontal resolution.

569 Although our focus here has been on the stratospheric transport circulation, mo-  
 570 tivating our use of tracer-independent metrics like the age-of-air, our results have clear

571 implications for constituent transport in GEOS-R21C. In particular, we showed that the  
572 increased age-of-air biases correspond to increased biases in the representations of CH<sub>4</sub>  
573 and N<sub>2</sub>O moving from the CCM1 Phase 1 to Phase 2 model configuration. This com-  
574 ports with well-known correlations between the mean age and stratospheric trace gases,  
575 reinforcing the fact that model transport inaccuracies continue to significantly affect sim-  
576 ulations of important long-lived chemical species in the stratosphere (Hall et al. (1999)).

577 Our results highlight the key role played by model numerics in transport (e.g., Rood  
578 (1987)). The sensitivities in the age-of-air documented herein are also consistent in spirit  
579 with the findings in Gupta et al. (2020) who showed significant age differences occurring  
580 between spectral versus finite-volume numerics. Our results, however, suggest that there  
581 remain large sensitivities even within a given (FV) dynamical core. Furthermore, we also  
582 show that that statistics derived from long AMIPs also manifest within a data assim-  
583 ilation context, which raises important questions as to the degree to which model biases  
584 can be ameliorated through assimilation of observations.

585 Looking forward, our findings support and build on the recommendation proposed  
586 in Gupta et al. (2020) for the construction of dynamical core benchmark tests aimed at  
587 determining how underlying AGCM numerics impact climatological transport proper-  
588 ties. In particular, in addition to the age-of-air, the authors propose a range of strato-  
589 spheric circulation diagnostics that should be evaluated including the zonal mean zonal  
590 winds, eddy temperature variance and zonal spectra of eddy kinetic energy. Our anal-  
591 ysis reveals an important role to be played by the climatological zonal mean wind struc-  
592 ture as it impacts wave convergence over midlatitudes; we therefore also recommend ex-  
593 plicit consideration of the Eliassen Palm flux convergence and tropical upwelling ( $w^*$ )  
594 fields as they may be crucial for interpreting age-of-air changes.

595 One somewhat incidental – but practical - result from our analysis is that the statis-  
596 tics of  $\nabla \cdot F$  and  $w^*$  are well approximated by ensembles of so-called EMIP integrations.  
597 As these are substantially easier to run than AMIPs these could provide a “first pass”  
598 when evaluating new proposed model development changes, without the immediate need  
599 to integrate AMIP-style experiments. We emphasize, however, that this statement should  
600 only apply to a first stage in model development as the age-of-air will reflect the time  
601 integrated impacts of both advection and mixing.

602 Finally, we conclude by noting that, while we have focused on sensitivities within  
603 the FV remapping algorithm, our results have highlighted important sensitivities to changes  
604 in radiation and, to a lesser extent, changes in parameterized convection. Though not  
605 the dominant drivers of the age-of-air changes identified here, the former could poten-  
606 tially influence the age both directly through changes in thermal structure and indirectly  
607 by modifying wave propagation and/or generation in the troposphere. Future work will  
608 focus on examining these impacts.

## PLACEHOLDER

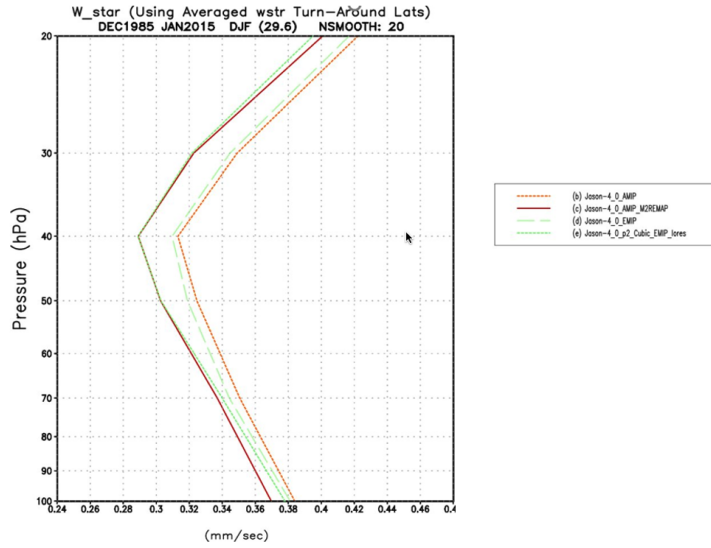


**Figure A1.** The DJF climatological mean vertical residual mean velocity,  $w^*$ , averaged between the turnaround latitudes for the CUBIC experiment (Table 2, row 7) (? colored line) and a CUBIC experiment performed using T, not TE, denoted CUBIC-T (? colored line). Results are based on 30-member ensemble EMIP experiments.

609  
610

## Appendix A Sensitivity of REMAP to Temperature (T) vs. Total Energy (TE)

611  
612  
613  
614  
615  
616  
617  
618  
619  
620

Whereas the modeling experiments listed in Table 2 (rows 5-7) focus on the sensitivity of Step 5 in REMAP Option 1 to the choice of interpolation scheme, another difference between REMAP Options 1 and 2 is the use of TE versus T, respectively. To test the impact of this difference, we ran a new experiment (CUBIC-T) which is identical to the CUBIC experiment (Table 2, row 7), except that T is remapped from input layer mean pressure locations to standard output layer mean locations directly using cubic interpolation (i.e., no computation of TE or a-posteriori energy conservation applied). Appendix Figure A1 shows that this has little impact on the strength of tropical upwelling, suggesting that the  $w^*$  differences between REMAP Options 1 and 2 are dominated by sensitivities to the choice of interpolation scheme, not the use of TE versus T.

621

## Appendix B Correspondence between EMIP and AMIP $w^*$

622  
623  
624

Appendix Figure B1 shows the close correspondence in DJF climatological mean  $w^*$ , averaged between the turnaround latitudes, from AMIP and EMIP experiments using the CUBIC configuration.

625

## Appendix C Changes in Tropical and High Latitude Upwelling

626  
627  
628

Appendix Figure C1 compares the behavior in residual mean upwelling among the LINEAR, QUADRATIC and CUBIC experiments over the latitudes between the (tropical) turnaround latitudes (left) and poleward of the northern turnaround latitude (right).

## PLACEHOLDER

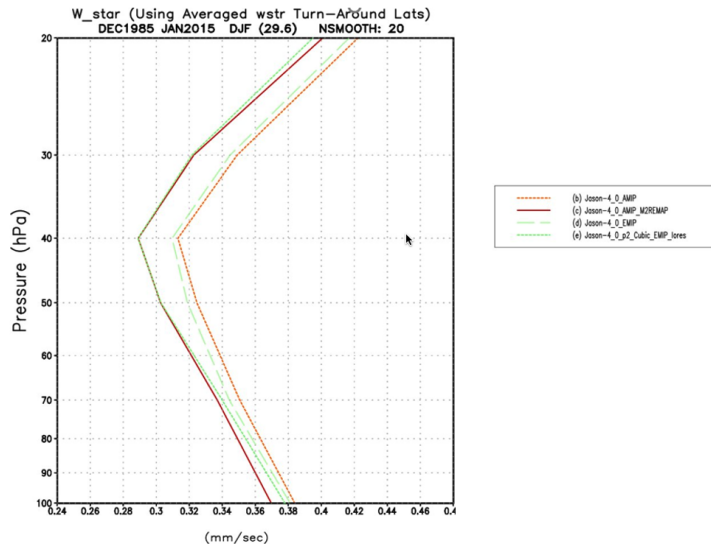


**Figure B1.** PLACEHOLDER FIGURE: The DJF climatological mean vertical residual mean velocity,  $w^*$ , averaged between the turnaround latitudes for the CTRL experiment (Table 2, row 1). Results based on a 30-year-long AMIP experiment (dotted orange line) and a 30-member ensemble of three-month-long EMIP experiments (dashed green line) are shown.

629 The ordering among experiments in both regions reflects how increases in downwelling  
 630 at high latitudes are, through mass balance, accompanied by enhanced upwelling in the  
 631 tropics.

## 632 Appendix D Tropopause Pressures

633 Appendix Figure D1 compares boreal winter tropopause pressures among the LIN-  
 634 EAR, QUADRATIC and CUBIC experiments, relative to MERRA-2.

## 635 Open Research Section

636 TBD

## 637 Acknowledgments

638 TBD

## 639 References

- 640 Abalos, M., Calvo, N., Benito-Barca, S., Garny, H., Hardiman, S. C., Lin, P., . . .  
 641 others (2021). The brewer–dobson circulation in cmip6. *Atmospheric Chem-*  
 642 *istry and Physics*, 21(17), 13571–13591.  
 643 Abalos, M., Orbe, C., Kinnison, D. E., Plummer, D., Oman, L. D., Jöckel, P., . . .  
 644 others (2020). Future trends in stratosphere-to-troposphere transport in ccmi



### DJF Climatological Mean Upwelling ( $w^*$ )

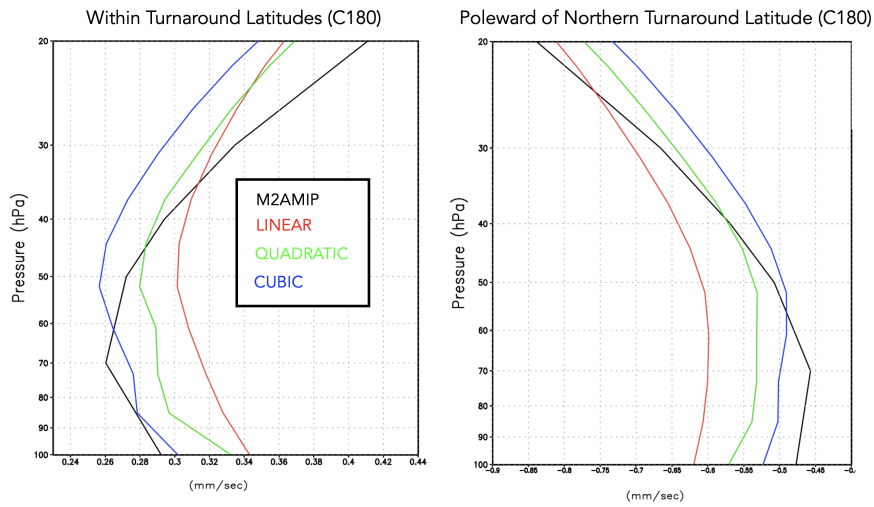


**Figure C1.** Left: The DJF climatological mean vertical residual mean velocity,  $w^*$ , averaged between the turnaround latitudes for the CTRL (cyan line; Table 2, row 1), LINEAR (green line; Table 2, row 5), and QUADRATIC (blue line; Table 2, row 6) experiments. M2AMIP is shown in black. Right: As in left panel, except averaged over latitudes poleward of the northern turnaround latitude. Results are shown for C180 experiments. **Replace MERRA-2 black line with M2AMIP**

### C180 EMIP 30-yr DJF Climatology (Dec 1985 – Feb 2015)

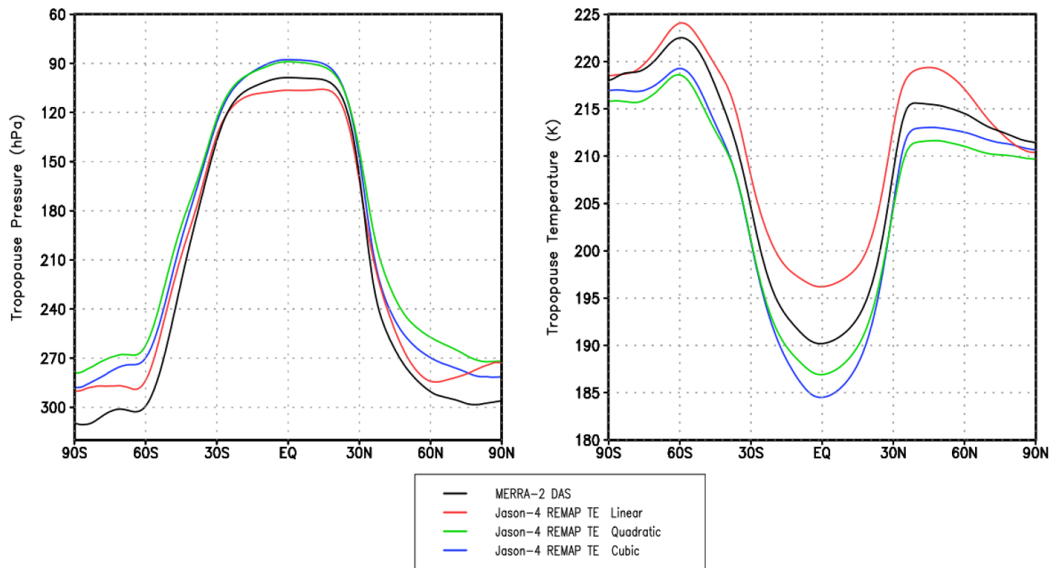


**Figure D1.** The DJF climatological mean tropopause pressure (left) and temperature (right) in the CUBIC (blue), QUADRATIC (green) and LINEAR (red) experiments. MERRA-2 is shown in black. Results are presented for the C180 experiments.

- 645 models. *Atmospheric Chemistry and Physics*, 20(11), 6883–6901.
- 646 Abalos, M., Randel, W. J., Kinnison, D. E., & Garcia, R. R. (2017). Using the arti-  
647 ficial tracer e90 to examine present and future utls tracer transport in waccm.  
648 *Journal of the Atmospheric Sciences*, 74(10), 3383–3403.
- 649 Andrews, D., Holton, J., & Leovy, C. (1987). Middle Atmosphere Dynam-  
650 ics. *Academic Press*, 60, 489. doi: 10.1175/1520-0469(2003)060<0103:  
651 CEOOAL>2.0.CO;2
- 652 Arnold, N. P., Putman, W. M., & Freitas, S. R. (2020). Impact of resolution and  
653 parameterized convection on the diurnal cycle of precipitation in a global  
654 nonhydrostatic model. *Journal of the Meteorological Society of Japan. Ser. II*.
- 655 Boering, K. A., Wofsy, S., Daube, B., Schneider, H., Loewenstein, M., Podolske, J.,  
656 & Conway, T. (1996). Stratospheric mean ages and transport rates from obser-  
657 vations of carbon dioxide and nitrous oxide. *Science*, 274(5291), 1340–1343.
- 658 Butchart, N., Cionni, I., Eyring, V., Shepherd, T., Waugh, D., Akiyoshi, H., ...  
659 others (2010). Chemistry–climate model simulations of twenty-first century  
660 stratospheric climate and circulation changes. *Journal of Climate*, 23(20),  
661 5349–5374.
- 662 Chiodo, G., & Polvani, L. M. (2019). The response of the ozone layer to quadru-  
663 pled co 2 concentrations: Implications for climate. *Journal of climate*, 32(22),  
664 7629–7642.
- 665 Chou, M.-D. (1990). Parameterizations for the absorption of solar radiation by o  
666 2 and co 2 with application to climate studies. *Journal of Climate*, 3(2), 209–  
667 217.
- 668 Chou, M.-D. (1992). A solar radiation model for use in climate studies. *Journal of*  
669 *Atmospheric Sciences*, 49(9), 762–772.
- 670 Chou, M.-D., & Suarez, M. J. (1994). An efficient thermal infrared radiation param-  
671 eterization for use in general circulation models.
- 672 Davis, N. A., Callaghan, P., Simpson, I. R., & Tilmes, S. (2022). Specified dynamics  
673 scheme impacts on wave-mean flow dynamics, convection, and tracer transport  
674 in cesm2 (waccm6). *Atmospheric Chemistry and Physics*, 22(1), 197–214.
- 675 Dietmüller, S., Eichinger, R., Garny, H., Birner, T., Boenisch, H., Pitari, G., ... oth-  
676 ers (2018). Quantifying the effect of mixing on the mean age of air in ccmval-2  
677 and ccmi-1 models. *Atmospheric Chemistry and Physics*, 18(9), 6699–6720.
- 678 Eichinger, R., Garny, H., Šácha, P., Danker, J., Dietmüller, S., & Oberländer-Hayn,  
679 S. (2020). Effects of missing gravity waves on stratospheric dynamics; part 1:  
680 climatology. *Climate Dynamics*, 54(5), 3165–3183.
- 681 Eluszkiewicz, J., Hemler, R. S., Mahlman, J. D., Bruhwiler, L., & Takacs, L. L.  
682 (2000). Sensitivity of age-of-air calculations to the choice of advection scheme.  
683 *Journal of the atmospheric sciences*, 57(19), 3185–3201.
- 684 Eyring, V., Lamarque, J.-F., Hess, P., Arfeuille, F., Bowman, K., Chipperfield,  
685 M. P., ... others (2013). Overview of igac/sparc chemistry-climate model  
686 initiative (ccmi) community simulations in support of upcoming ozone and  
687 climate assessments. *SPARC newsletter*, 40(Januar), 48–66.
- 688 Freitas, S. R., Grell, G. A., Molod, A., Thompson, M. A., Putman, W. M., Santos e  
689 Silva, C. M., & Souza, E. P. (2018). Assessing the grell-freitas convection  
690 parameterization in the nasa geos modeling system. *Journal of Advances in*  
691 *Modeling Earth Systems*, 10(6), 1266–1289.
- 692 Freitas, S. R., Putman, W. M., Arnold, N. P., Adams, D. K., & Grell, G. A. (2020).  
693 Cascading toward a kilometer-scale gcm: Impacts of a scale-aware convection  
694 parameterization in the goddard earth observing system gcm. *Geophysical*  
695 *Research Letters*, 47(17), e2020GL087682.
- 696 Gelaro, R., McCarty, W., Suárez, M. J., Todling, R., Molod, A., Takacs, L., ...  
697 others (2017). The modern-era retrospective analysis for research and applica-  
698 tions, version 2 (merra-2). *Journal of climate*, 30(14), 5419–5454.
- 699 Gerber, E. P., & Manzini, E. (2016). The dynamics and variability model intercom-

- 700        parison project (dynvarmip) for cmip6: assessing the stratosphere–troposphere  
701        system. *Geoscientific Model Development*, 9(9), 3413–3425.
- 702        Grell, G. A., & Freitas, S. R. (2014). A scale and aerosol aware stochastic convective  
703        parameterization for weather and air quality modeling. *Atmospheric Chemistry  
704        and Physics*, 14(10), 5233–5250.
- 705        Grooß, J.-U., & Russell III, J. M. (2005). A stratospheric climatology for o 3, h 2  
706        o, ch 4, no x, hcl and hf derived from haloe measurements. *Atmospheric chem-  
707        istry and physics*, 5(10), 2797–2807.
- 708        Gupta, A., Gerber, E. P., & Lauritzen, P. H. (2020). Numerical impacts on tracer  
709        transport: A proposed intercomparison test of atmospheric general circula-  
710        tion models. *Quarterly Journal of the Royal Meteorological Society*, 146(733),  
711        3937–3964.
- 712        Hall, T. M., & Plumb, R. A. (1994). Age as a diagnostic of stratospheric transport.  
713        *Journal of Geophysical Research: Atmospheres*, 99(D1), 1059–1070.
- 714        Hall, T. M., Waugh, D. W., Boering, K. A., & Plumb, R. A. (1999). Evaluation  
715        of transport in stratospheric models. *Journal of Geophysical Research: Atmo-  
716        spheres*, 104(D15), 18815–18839.
- 717        Hardiman, S. C., Andrews, D. G., White, A. A., Butchart, N., & Edmond, I. (2010).  
718        Using different formulations of the transformed eulerian mean equations and  
719        eliassen–palm diagnostics in general circulation models. *Journal of the atmo-  
720        spheric sciences*, 67(6), 1983–1995.
- 721        Hardiman, S. C., Butchart, N., & Calvo, N. (2014). The morphology of the brewer-  
722        dobson circulation and its response to climate change in cmip5 simulations.  
723        *Quarterly Journal of the Royal Meteorological Society*, 140(683), 1958–1965.
- 724        Haynes, P., McIntyre, M., Shepherd, T., Marks, C., & Shine, K. P. (1991). On the  
725        “downward control” of extratropical diabatic circulations by eddy-induced  
726        mean zonal forces. *Journal of the Atmospheric Sciences*, 48(4), 651–678.
- 727        Hegglin, M. I., Brunner, D., Peter, T., Hoor, P., Fischer, H., Staehelin, J., . . . Weers,  
728        U. (2006). Measurements of no, no y, n 2 o, and o 3 during spurt: implica-  
729        tions for transport and chemistry in the lowermost stratosphere. *Atmospheric  
730        chemistry and physics*, 6(5), 1331–1350.
- 731        Holton, J. R., Haynes, P. H., McIntyre, M. E., Douglass, A. R., Rood, R. B., & Pfs-  
732        ter, L. (1995). Stratosphere-troposphere exchange. *Reviews of geophysics*,  
733        33(4), 403–439.
- 734        Holzer, M., & Hall, T. M. (2000). Transit-time and tracer-age distributions in geo-  
735        physical flows. *Journal of the atmospheric sciences*, 57(21), 3539–3558.
- 736        Iacono, M. J., Delamere, J. S., Mlawer, E. J., Shephard, M. W., Clough, S. A., &  
737        Collins, W. D. (2008). Radiative forcing by long-lived greenhouse gases:  
738        Calculations with the aer radiative transfer models. *Journal of Geophysical  
739        Research: Atmospheres*, 113(D13).
- 740        Ivy, D. J., Solomon, S., Calvo, N., & Thompson, D. W. (2017). Observed connec-  
741        tions of arctic stratospheric ozone extremes to northern hemisphere surface  
742        climate. *Environmental Research Letters*, 12(2), 024004.
- 743        Kouatchou, J., Molod, A., Nielsen, J., Auer, B., Putman, W., & Clune, T. (2015).  
744        *Geos-5 chemistry transport model user’s guide* (Tech. Rep.).
- 745        Legras, B., Pisso, I., Berthet, G., & Lefèvre, F. (2004). Variability of the lagrangian  
746        turbulent diffusivity in the lower stratosphere. *Atmospheric Chemistry and  
747        Physics Discussions*, 4(6), 8285–8325.
- 748        Lin, S.-J. (2004). A “vertically lagrangian” finite-volume dynamical core for global  
749        models. *Monthly Weather Review*, 132(10), 2293–2307.
- 750        Molod, A., Takacs, L., Suarez, M., & Bacmeister, J. (2015). Development of the  
751        geos-5 atmospheric general circulation model: Evolution from merra to merra2.  
752        *Geoscientific Model Development*, 8(5), 1339–1356.
- 753        Monge-Sanz, B., Chipperfield, M., Simmons, A., & Uppala, S. (2007). Mean age of  
754        air and transport in a ctm: Comparison of different ecmwf analyses. *Geophys-*

- 755 *cal Research Letters*, 34(4).
- 756 Monge-Sanz, B. M., Bozzo, A., Byrne, N., Chipperfield, M. P., Diamantakis, M.,  
757 Flemming, J., ... others (2022). A stratospheric prognostic ozone for seam-  
758 less earth system models: performance, impacts and future. *Atmospheric*  
759 *Chemistry and Physics*, 22(7), 4277–4302.
- 760 Morgenstern, O., & Carver, G. D. (2001). Comparison of cross-tropopause transport  
761 and ozone in the upper troposphere and lower stratosphere region. *Journal of*  
762 *Geophysical Research: Atmospheres*, 106(D10), 10205–10221.
- 763 Neu, J., Strahan, S., Braesicke, P., Douglass, A., Huck, P., Oman, L., ... Tegtmeier,  
764 S. (2010). Sparc ccmval (2010), sparc report on the evaluation of chemistry-  
765 climate models: Chapter 5: Transport. SPARC.
- 766 Neu, J. L., & Plumb, R. A. (1999). Age of air in a “leaky pipe” model of strato-  
767 spheric transport. *Journal of Geophysical Research: Atmospheres*, 104(D16),  
768 19243–19255.
- 769 Oehrlein, J., Chiodo, G., & Polvani, L. M. (2020). The effect of interactive ozone  
770 chemistry on weak and strong stratospheric polar vortex events. *Atmospheric*  
771 *Chemistry and Physics*, 20(17), 10531–10544.
- 772 Orbe, C., Oman, L. D., Strahan, S. E., Waugh, D. W., Pawson, S., Takacs, L. L., &  
773 Molod, A. M. (2017). Large-scale atmospheric transport in geos replay simula-  
774 tions. *Journal of Advances in Modeling Earth Systems*, 9(7), 2545–2560.
- 775 Orbe, C., Rind, D., Jonas, J., Nazarenko, L., Faluvegi, G., Murray, L. T., ... oth-  
776 ers (2020). Giss model e2. 2: A climate model optimized for the middle  
777 atmosphere—2. validation of large-scale transport and evaluation of cli-  
778 mate response. *Journal of Geophysical Research: Atmospheres*, 125(24),  
779 e2020JD033151.
- 780 Orbe, C., Yang, H., Waugh, D. W., Zeng, G., Morgenstern, O., Kinnison, D. E., ...  
781 others (2018). Large-scale tropospheric transport in the chemistry–climate  
782 model initiative (ccmi) simulations. *Atmospheric Chemistry and Physics*,  
783 18(10), 7217–7235.
- 784 Pan, L. L., Wei, J., Kinnison, D., Garcia, R., Wuebbles, D., & Brasseur, G. P.  
785 (2007). A set of diagnostics for evaluating chemistry-climate models in the ex-  
786 tratropical tropopause region. *Journal of Geophysical Research: Atmospheres*,  
787 112(D9).
- 788 Pawson, S., Stajner, I., Kawa, S. R., Hayashi, H., Tan, W.-W., Nielsen, J. E., ...  
789 Livesey, N. J. (2007). Stratospheric transport using 6-h-averaged winds from  
790 a data assimilation system. *Journal of Geophysical Research: Atmospheres*,  
791 112(D23).
- 792 Plumb, R. A. (1985). On the three-dimensional propagation of stationary waves.  
793 *Journal of Atmospheric Sciences*, 42(3), 217–229.
- 794 Plumb, R. A. (1996). A “tropical pipe” model of stratospheric transport. *Journal of*  
795 *Geophysical Research: Atmospheres*, 101(D2), 3957–3972.
- 796 Plumb, R. A. (2002). Stratospheric transport. *Journal of the Meteorological Society*  
797 *of Japan. Ser. II*, 80(4B), 793–809.
- 798 Polvani, L. M., Waugh, D. W., Correa, G. J., & Son, S.-W. (2011). Stratospheric  
799 ozone depletion: The main driver of twentieth-century atmospheric circulation  
800 changes in the southern hemisphere. *Journal of Climate*, 24(3), 795–812.
- 801 Prather, M. J., Zhu, X., Tang, Q., Hsu, J., & Neu, J. L. (2011). An atmospheric  
802 chemist in search of the tropopause. *Journal of Geophysical Research: Atmo-*  
803 *spheres*, 116(D4).
- 804 Rood, R. B. (1987). Numerical advection algorithms and their role in atmospheric  
805 transport and chemistry models. *Reviews of geophysics*, 25(1), 71–100.
- 806 Rosenlof, K. H. (1995). Seasonal cycle of the residual mean meridional circulation  
807 in the stratosphere. *Journal of Geophysical Research: Atmospheres*, 100(D3),  
808 5173–5191.
- 809 Son, S.-W., Tandon, N. F., Polvani, L. M., & Waugh, D. W. (2009). Ozone hole and

- 810 southern hemisphere climate change. *Geophysical Research Letters*, *36*(15).  
811 Strahan, S., Douglass, A., & Newman, P. (2013). The contributions of chemistry  
812 and transport to low arctic ozone in march 2011 derived from aura mls obser-  
813 vations. *Journal of Geophysical Research: Atmospheres*, *118*(3), 1563–1576.  
814 Thiele, G., & Sarmiento, J. (1990). Tracer dating and ocean ventilation. *Journal of*  
815 *Geophysical Research: Oceans*, *95*(C6), 9377–9391.  
816 Waugh, D., & Hall, T. (2002). Age of stratospheric air: Theory, observations, and  
817 models. *Reviews of Geophysics*, *40*(4), 1–1.